Overview of Physics Results from MAST

B. Lloyd[1], R.J. Akers[1], F. Alladio[2], Y. Andrew[1], L.C. Appel[1], D. Applegate[1], K.B. Axon[1], N. Ben Ayed[3], C. Bunting[1], R.J. Buttery[1], P.G. Carolan[1], I. Chapman[1], D. Ciric[1], J.W. Connor[1], N.J. Conway[1], M. Cox[1], G.F. Counsell[1], G. Cunningham[1], A. Darke[1], E. Delchambre[1], R.O. Dendy[1], J. Dowling[1], B. Dudson[4], M. Dunstan[1], A.R. Field[1], A. Foster[5], S. Gee[1], L. Garzotti[1], M.P. Gryaznevich[1], A. Gurchenko[6], E. Gusakov[6], N.C. Hawkes[1], P. Helander[1], T.C. Hender[1], B. Hnat[7], D.F. Howell[1], N. Joiner[8], D. Keeling[1], A. Kirk[1], B. Koch[9], M. Kuldkepp[10], S. Lisgo[11], F. Lott[8], G.P. Maddison[1], R. Maingi[12], A. Mancuso[2], S.J. Manhood[1], R. Martin[1], G.J. McArdle[1], J. McCone[13], H. Meyer[1], P. Micozzi[2], A.W. Morris[1], D.G. Muir[1], M. Nelson[14], M.R. O'Brien[1], A. Patel[1], S. Pinches[1], J. Preinhaelter[15], M.N. Price[1], E. Rachlew[10], C.M. Roach[1], V. Rozhansky[16], S. Saarelma[1], A. Saveliev[6], R. Scannell[13], S.E. Sharapov[1], V. Shevchenko[1], S. Shibaev[1], K. Stammers[1], J. Storrs[1], A. Surkov[6], A. Sykes[1], S. Tallents[8], D. Taylor[1], N. Thomas-Davies[1], M.R. Turnyanskiy[1], J. Urban[15], M. Valovic[1], R.G.L. Vann[3], F. Volpe[1], G. Voss[1], M.J. Walsh[1], S.E.V. Warder[1], R. Watkins[1], H.R. Wilson[3], M. Wisse[13] and the MAST and NBI teams.

[1]EURATOM/UKAEA Fusion Association, Culham Science Centre, Abingdon, UK
[2]Associazione EURATOM-ENEA sulla Fusione, Frascati, Rome, Italy
[3]University of York, Heslington, York, UK
[4]Oxford University, Clarendon Laboratory, Oxford, UK.
[5]University of Strathclyde, Glasgow, UK.
[6]A.F. Ioffe Physico-Technical Institute, St. Petersburg, Russia.
[7]Department of Physics, Warwick University, UK.
[8]Imperial College of Science, Technology and Medicine, London, UK.
[9]Institut für Physik der Humboldt, Universität zu Berlin, Germany.
[10]Dept. of Physics, KTH, EURATOM -VR Association, Stockholm, Sweden.
[11]University of Toronto Institute for Aerospace Studies, Toronto, Canada.
[12]Oak Ridge National Laboratory, Oak Ridge, USA.
[13]University College, Cork, Association EURATOM-DCU Ireland.
[14]Queen's University, Belfast, UK.
[15]EURATOM/IPP.CR Fusion Association, Prague, Czech Republic.
[16]St. Petersburg State Polytechnical University, St. Petersburg, Russia.
e-mail contact of main author: brian.lloyd@ukaea.org.uk

Abstract. Substantial advances have been made on MAST. The parameter range of the MAST confinement database has been extended and it now also includes pellet-fuelled discharges. Good pellet retention has been observed in H-mode discharges without triggering an ELM or an H/L transition. Co-ordinated studies on MAST and DIII-D demonstrate a strong link between the aspect ratio and beta scaling of H-mode energy confinement, consistent with that obtained when MAST data were merged with a subset of the ITPA database. Electron and ion ITBs are readily formed and their evolution has been investigated. Electron and ion thermal diffusivities have been reduced to values close to the ion neoclassical level. Error field correction coils have been used to determine the locked mode threshold scaling which is comparable to that in conventional aspect ratio tokamaks. The impact of plasma rotation on sawteeth has been investigated and the results have been well-modelled using the MISHKA-F code. Alfvén cascades have been observed in discharges with reversed magnetic shear. Measurements during off-axis NBCD and heating are consistent with classical fast ion modelling and indicate efficient heating and significant driven current. Electron Bernstein wave heating has been observed via the O-X-B mode conversion process. Plasmas with low pedestal collisionality have been established and further insight has been gained into the characteristics of filamentary structures at the plasma edge. Complex behaviour of the divertor power loading during plasma disruptions has been revealed by high resolution infra-red measurements.

1. Introduction

The Mega Ampère Spherical Tokamak (MAST) is designed to study low aspect ratio (R/a ~ 0.85m/0.65m ~1.3), highly elongated ($\kappa > 2$), high temperature plasmas in order to: (i) explore the long term potential of the ST as a Component Test Facility (CTF) or ST power plant and (ii) address key tokamak physics issues for ITER and DEMO. In order to achieve these aims, MAST is equipped with extensive and advanced diagnostics, a digital control system, error field correction coils, adaptable fuelling systems and both neutral beam and electron Bernstein wave heating systems. Notable diagnostic capabilities include very high spatial and temporal resolution kinetic measurements (Thomson scattering (TS), 2D visible bremsstrahlung for Z_{eff}, and CXRS for toroidal/poloidal rotation plus ion temperature measurements with a spatial resolution comparable to the ion Larmor radius); fast wide-angle imaging systems (visible, infra-red) which fully exploit the unique diagnostic access in MAST; high frequency (5MHz) magnetic measurements; and a comprehensive suite of plasma edge diagnostics. These capabilities allow kinetically constrained EFIT calculations, incorporating plasma rotation, to be deployed for equilibrium reconstruction. During the last two years, first results have been obtained from a new edge TS system providing high resolution measurements in the pedestal and near scrape-off layer (SOL) down to ~ 5eV, multi-wavelength/narrow bandwidth imaging systems viewing the divertor and the injected neutral beams, new edge probes and a prototype Motional Stark Effect (MSE) system for q profile measurements. The digital plasma control system incorporates density feedback control and a novel optical system for plasma radial position control. Real-time equilibrium reconstruction, based on RTEFIT, has been successfully deployed in the control system. Improvements to the vertical position control system now allow operation up to plasma elongation $\kappa \sim 2.6$. To allow higher power, longer pulse, operation, the MAST divertor was upgraded in 2004 and the two short pulse neutral beam injectors are presently being upgraded to long pulse JET-style PINI sources. The first PINI is now being commissioned and has operated into MAST at a power level ~ 1MW (ultimately 2.5MW).

2. Confinement and Transport

2.1. Confinement Scaling

The MAST confinement database, which includes both L-mode and H-mode plasmas, has recently been extended to higher I_p, lower n_e and now includes discharges fuelled by deuterium pellets (section 2.4). Further submission of MAST data to the ITPA H-mode confinement database has quadrupled the number of MAST data points. MAST H-mode data broadly agree with the IPB98y2 energy confinement scaling, but the L-mode scaling, L97, generally underestimates confinement in MAST L-mode plasmas [1], suggesting a more positive dependence on inverse aspect ratio than given by the scaling. A dedicated plasma current scan (I_p = 0.6 - 1.2 MA) in L-mode, at constant density, showed that the scaling of energy confinement time with plasma current is similar to that given by L97 ($\tau_E \propto I_p^{0.96}$). At 1.2MA, T_{i0} and T_{e0} reached 3keV and 2keV respectively, for an injected power < 2MW (Fig. 1). High current (1.2MA) H-mode operation has also been established recently in MAST and will be used to establish the scaling of energy confinement with plasma current in H-mode.

Data from spherical tokamaks significantly extend the range of the inverse aspect ratio (ε=a/R) and thermal toroidal beta β in the ITPA H-mode confinement database [1]. The

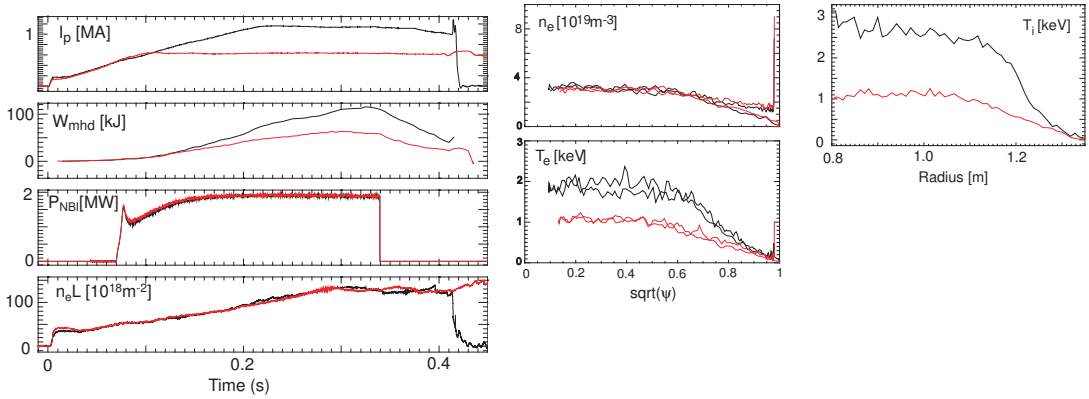

FIG. 1. L-mode plasma current scan (I_p = 0.6 – 1.2 MA). Plasma current, total energy, NBI power and line-integrated density are shown as well as temperature and density profiles close to the beam turn-off time(#14625, #14626).

correlation between these dimensionless parameters introduces an interplay between the β and ε scalings [1, 2]. It has been shown [1] that merging of MAST data with the international database, assuming gyro-Bohm scaling with β degradation and no collisionality dependence, gives an aspect ratio dependence of the form $B\tau_E \propto \rho_*^{-3}\beta^{-1}\varepsilon^{0.77\pm0.3}$, i. e. similar to the dimensionless form of the IPB98y2 scaling. However, if it is assumed that the scaling is independent of β, then the dependence becomes $B\tau_E \propto \rho_*^{-3}\beta^{0}\varepsilon^{-0.63\pm0.2}$. To examine this effect more closely, dedicated experiments have been performed on MAST and DIII-D, matching the plasma shape, safety factor, poloidal beta and normalised poloidal Larmor radius and thereby yielding a powerful constraint on the exponents in the dimensionless energy confinement scaling law: $B\tau_{Eth} \propto \rho_*^{x_\rho}\beta^{x_\beta}\nu_*^{x_\nu}\varepsilon^{x_\varepsilon}M^{x_M}q^{x_q}\kappa^{x_\kappa}$ in the form of:

$$-2.92 = 0.95x_\rho + 1.57x_\beta - 2.56x_\nu + x_\varepsilon$$

This constraint is consistent with gyro-Bohm scaling ($x_\rho = -3$), weakly favourable collisionality scaling, as observed in MAST [1] and other devices, and a β and ε interplay consistent with that derived from the database analysis [1, 2].

2.2. H-mode Access and Control

High confinement (H-mode) regimes are readily accessed in MAST with co- or counter-NBI, in DND or SND configurations, and also in Ohmically heated plasmas. It has been shown that H-mode access is improved with inboard fuelling [3]. In order to understand this effect further, the influence of the gas-puff rate on the edge radial electric field in Ohmic L-mode plasmas has been studied. Measured changes in the toroidal impurity flow of He^+ ions with increasing high-field-side gas-puff rate indicated an increase of the magnitude of the negative radial electric field, as predicted by B2SOLPS5.0 modelling [4].

The dependence of H-mode threshold power, P_{th}, on the position of the X-point with respect to the ion grad-B drift in single null plasmas is well-established. However, it has been shown in MAST that a reduction in P_{th} can be achieved in double null configurations if the two X-points are almost on the same flux surface [5]. This effect is more pronounced in spherical tokamaks such as MAST and NSTX, than in conventional tokamaks such as AUG [6]. The strong dependence of P_{th} on the balance of the magnetic configuration close to 'connected' double null (C-DN) in MAST can be exploited to control L-to-H and H-to-L transitions [7]. Repeated short, $\Delta t < 20$ ms, L-mode phases can be triggered in H-mode plasmas by controlled

upward shifts of a C-DN plasma ($\delta r_{sep} \approx 0$ mm) to an upper single null (U-SN) configuration ($\delta r_{sep} > 8$ mm); δr_{sep} is the radial separation of the two separatrices at the outboard mid-plane. At the H to L transition the radial electric field E_r collapses in $\Delta t = (300 \pm 100)$ μs causing the He^+ velocity to change by ~20 km/s. Infra-red measurements show that the forced H-to-L transition results in a lower peak power loading on the divertor targets than observed during ELMs. The physics of the reduced P_{th} in the C-DN configuration is probably related to the change of the SOL flow pattern. In L-mode discharges a difference of $\Delta E_r \approx -1 kV/m$ between C-DN and lower single null (L-SN) with the ion grad-B drift towards the X-point has been observed on MAST and AUG [6]. A larger change of E_r is observed between L-SN and U-SN. These variations agree well with B2SOLPS5.0 simulations [8]. There is also strong evidence that a shorter outer divertor leg length leads to a lower P_{th} in MAST, consistent with results from JET [9].

2.3. Transport Studies

The comprehensive array of high resolution kinetic diagnostics on MAST (see section 1), combined with sophisticated transport analysis and turbulence codes (e.g. TRANSP, the gyrokinetic code GS2, the two fluid code CUTIE etc.) provide an excellent basis for detailed transport studies. MAST plasmas are generally characterised by high ExB flow shear, to which the toroidal rotation driven by the NBI torque is the dominant contributor. As a result, internal transport barriers (ITBs) are readily formed, especially in the ion channel. In typical H-mode plasmas, χ_i and χ_e can approach the ion neoclassical level around mid-radius and extending towards the plasma boundary, where the high shearing rate ω_{SE} is maintained. In L-mode plasmas, χ_i and χ_e around mid-radius are similar in absolute magnitude to the H-mode values (although there is a stronger enhancement over the ion neoclassical level) but they typically increase significantly towards the plasma boundary. The inferred momentum diffusivity is typically of order $\chi_\phi \sim \chi_i$ in MAST, but in enhanced confinement regimes $\chi_\phi/\chi_i < 1$ with the strongest reduction in this ratio occurring for counter-NBI where the Ware pinch and an inwards NBI driven pinch can be significant [10]. Linear microstability studies, both analytically and using GS2, are improving our understanding of ITG, ETG, TEM, KBM, microtearing and ubiquitous modes in MAST [11]. Non-linear GS2 calculations for a typical MAST H-mode plasma indicate the presence of radially extended (~ $100\rho_e$) electrostatic streamers giving rise to a calculated thermal diffusivity around mid-radius of ~ $5 m^2/s$ [11], close to typical experimental values. For counter-NBI, where the contribution of the driven toroidal flow to the ExB flow shear augments that due to the ion pressure gradient, very high shearing rates are observed ($\omega_{SE} \sim 10^6 s^{-1}$), far exceeding the ITG growth rate. Previous measurements have shown the presence of steep electron transport barriers in such discharges. In the region of the electron transport barrier

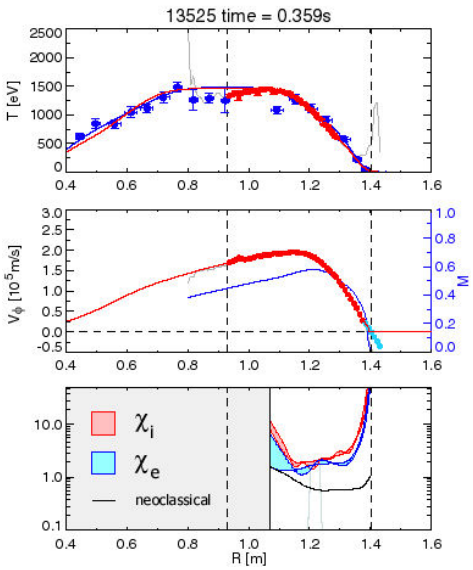

Fig. 2 Temperature and rotation profiles and thermal diffusivities χ_i, χ_e, χ_i^{neo} (TRANSP) for counter-NBI discharge #13525

long wavelength TEM modes are predicted to be stabilised [11]. Further improvements in the spatial and temporal resolution of CXRS measurements have enabled us to confirm the existence of an ion barrier in these counter-NBI discharges and, together with Thomson scattering measurements, to measure the temporal evolution of the ion and electron transport barriers in both co and counter-NBI discharges. In both cases, barriers are formed in the core then broaden substantially and weaken as the discharge evolves. In the counter-NBI case, where a high shearing rate can be sustained across most of the plasma profile, thermal diffusivities fall to $\chi_i \sim \chi_e \sim 2m^2/s$ over a wide region (Fig. 2).

2.4. Pellet Fuelling

MAST is equipped with an eight barrel (six currently in service) gas-propulsion pellet launcher. Pellets can be injected either radially, from an outboard mid-plane port, or through a top port, which directs them vertically through the plasma inboard side, with velocities up to ~ 600m/s. Fuelling efficiencies are similar for outboard and top-inboard launch [12]. Recent experiments have focussed on the study of pellet deposition physics and post-pellet losses in beam heated H-mode DND plasmas, where pellets of size equal to 20-40% of the plasma content were injected from the top-inboard position with velocities in the range 240 – 450m/s, depositing particles in the outer part of the plasma (r/a > 0.7). The ablation process lasts ~ 2ms and is diagnosed by fast visible imaging (multiple locations), bremsstrahlung emission and Thomson scattering, including the high spatial resolution ruby laser system (300 points covering the whole plasma diameter) triggered, with variable delay, by the pellet (Fig. 3). Post-pellet profiles can be well reproduced by the neutral gas shielding model [13,14], but this is not always the case. Further analysis, and comparison with various models, is being carried out in order to understand better the ablation process and the role of drifts. An energy confinement database has been created using discharges for which pellets increase the plasma density by a factor of ~ 2 in the outer ~ 30% of the plasma minor radius - the situation expected in future devices. First data indicate that the confinement penalty for pellet fuelling is ~10%, similar to that observed in JET. Although pellets can induce ELMs or an H/L transition, typical behaviour in conventional tokamaks, there are many examples where the discharges remain in H-mode, ELMs are not triggered and there is good retention of the pellet fuelling (Fig. 4). This may be linked to a favourable effect of the strong shaping in spherical tokamaks.

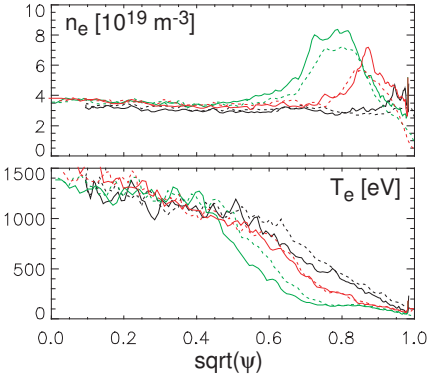

FIG. 3. TS measurements of $n_e(r)$ and $T_e(r)$ near the beginning (black), middle (red) and end (green) of the (2ms) pellet ablation process, for similar sized pellets launched from the top-inboard (v=380m/s) into NBI-heated H-mode. Solid (dashed) profiles measured simultaneously at the inboard (outboard) side(#12958, #12959, #12961).

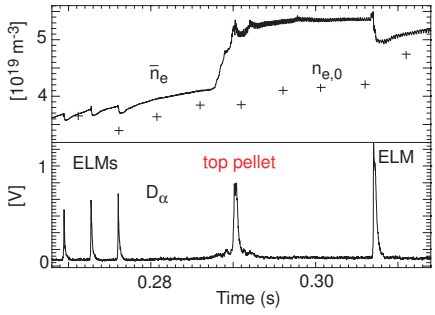

FIG. 4. Density and D_α signals for shallow pellet injection into an NBI heated H-mode plasma showing good pellet retention and no back-transition or triggering of ELMs (#12794).

3. Heating, Current Drive and Start-up

3.1. Neutral Beam Heating and Current Drive

Future STs rely upon a large pressure driven current plus off-axis auxiliary current drive for optimum performance. Recent studies have therefore focussed on evaluation of neutral beam heating and current drive capability for different injection geometries [15]. Data are modelled using TRANSP and LOCUST. The excellent agreement of modelling with experimental data over a wide range of conditions [16] indicates that the beam ion population evolves predominantly due to Coulomb collisions and charge exchange phenomena, and confirms the classical behaviour of the fast ions. The flexibility offered by the large MAST vessel has been exploited for preliminary studies of *off-axis* heating and current drive in vertically displaced SND plasmas [17] with beam deposition at about half minor radius. Efficient off-axis heating is observed, comparable to up-down symmetric DND discharges with on-axis NBI. For an injected power of 1.7MW, T_{e0} and T_{i0} increase from ~ 0.5keV to ~ 1.5keV. The observed heating efficiency is the same in upper (U) and lower (L) SND plasmas. However, in the case of L-SND, the appearance of the q=1 surface (EFIT) and onset of sawtoothing are delayed compared with U-SND and the plasma internal inductance is lower. These observations are consistent with a larger off-axis driven current in the case of L-SND as expected theoretically. The ratio B_θ / B_ϕ is not small in MAST and results in a higher population of trapped ions in the U-SND discharges, as confirmed by NPA measurements. In conventional tokamaks, where $B_\phi >> B_\theta$, this effect is negligible. TRANSP analyses exhibit an excellent match to the experimental data and indicate an NBCD fraction of up to 25% (Fig. 5).

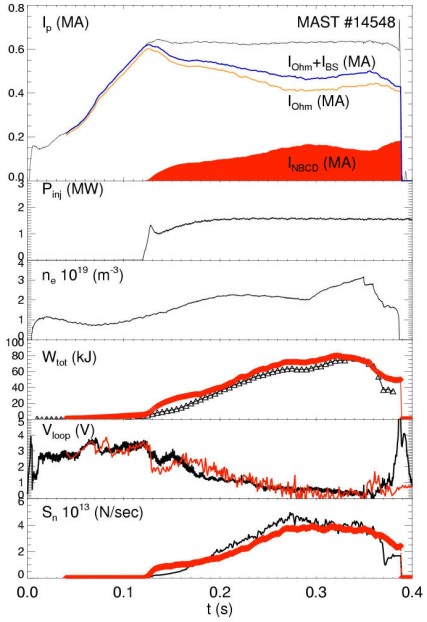

FIG. 5. Plasma current, NBI power, line-averaged density, plama energy, loop voltage and neutron yield during off-axis NBI (L-SND). TRANSP simulations are shown in colour.

3.2. Electron Bernstein Wave Heating

Electron Bernstein waves (EBW), which can be excited by the so-called O-X-B mode conversion process, can potentially provide efficient heating and current drive in ST plasmas, both in the core and off-axis. Efficient mode conversion from the launched ordinary (O) mode to the extra-ordinary (X) mode occurs for a narrow range of launch angles around the optimum, requiring accurate control of the launched beams. The resulting X-mode subsequently converts to the Bernstein (B) wave in the vicinity of the upper hybrid resonance. Measurement of 'EBW emission', via the inverse B-X-O mode conversion process, has been used on MAST to confirm theoretical predictions and to identify the optimum conditions for efficient heating and current drive via the O-X-B process. In addition, major advances in

integrated modelling of EBW heating and current drive have recently been achieved using a suite of codes [18]. Both emission measurements and modelling indicate that the preferred frequency for EBW heating and current drive in MAST lies in the range 16 – 28GHz. The existing 60GHz, 1.4MW gyrotron complex, whilst not at the optimum frequency for MAST, has allowed proof-of-principle experiments to be carried out at power levels up to 0.8MW. An antenna equipped with 21 mirrors (14 of which are moveable) allows accurate control of poloidal and toroidal launch angles as well as the polarisation of up to 7 launched beams. Because of the relatively high frequency, the requirements on target plasma parameters are stringent and the mode conversion window is particularly narrow. Nevertheless, EBW heating has been observed in several regimes [18]. For example, core heating $(\Delta T_{e0} / T_{e0} \sim 10\%)$ has been observed in high density $\left(\overline{n}_e \sim 2-3\times10^{20}\, m^{-3}\right)$ Ohmic H-mode plasmas compressed to smaller major radius/higher magnetic field. In ELM-free H-mode discharges with steep edge gradient, EBW absorption is very peripheral (r/a ~ 0.9), the O-X-B conversion occurs in relatively cold plasma and parametric decay phenomena are observed. Comparison with calculated parametric decay power thresholds indicates a mode conversion efficiency ≥ 50% for at least one of the beams [19], since there is no beam overlap.

3.3. Start-up Studies

Plasma initiation and current ramp-up without using central solenoid flux is a key area of ST research, due to the difficulty of providing adequate neutron shielding of a solenoid in an ST power plant or CTF. Various non-solenoid start-up schemes have been deployed in MAST, generating plasma currents up to 0.5MA. Recent detailed modelling [20] has provided a better understanding of these schemes. ECRH pre-ionisation has also been used effectively in MAST. It was estimated theoretically, and confirmed experimentally, that at 60GHz the minimum RF breakdown field is about 1.5kV/cm over a wide range of connection lengths and gas pressures. A dedicated 28GHz, 200kW, start-up system, based on EBW excitation, is presently being installed in MAST.

4. Plasma Stability

4.1. Locked Mode Threshold Studies

Non-axisymmetric magnetic fields, or error fields, caused by small imperfections and/or misalignments of field coils, can lead to 'locked' modes, resulting in early plasma termination. MAST is equipped with a set of four error field correction coils, allowing the application of a predominantly n = 1 spectrum at an arbitrary toroidal phase, designed to compensate the intrinsic error field. Correction of the intrinsic error field has allowed MAST to operate in previously inaccessible regimes [21]. Experiments have been performed to investigate how the m = 2, n = 1 radial magnetic field required to form a locked mode scales with density, toroidal field and q. It was found that the locked mode threshold, expressed in terms of the m = 2, n = 1 component of the field normal to the q = 2 surface, can be written $B_{21} / B_T = 5.10^{-5}\, \overline{n}_e^{1.1\pm0.2} B_T^{-0.7\pm0.1} q_{cyl}^{1.4\pm0.2}$ where the toroidal field B_T is in T, the line-averaged density $\overline{n}_e$ is in units of 10^{19}m^{-3} and $q_{cyl} = (2\pi a^2 B_T)/(R\mu_0 I_p)$. This scaling is in reasonable agreement with those found in conventional aspect ratio tokamaks. In order to determine if there is an aspect ratio effect on the locked mode threshold, a set of MAST experiments was carried out in discharges for which $\overline{n}_e$ and q_{95} were matched as closely as possible to those

used in DIII-D studies. The plasma cross-section and applied n = 1 error field spectrum are well matched in the two devices. If we assume an extended power law scaling, including the aspect ratio $B_{21}/B_T \propto \overline{n}_e (R/a)^{\alpha_A}$ then $-0.3 \le \alpha_A \le 0.3$ where the residual uncertainty arises from differences in the scaling with toroidal field and q in the two devices.

4.2. The Effect of Toroidal Plasma Rotation on Sawteeth

Sawtooth control is important for optimisation of plasma performance. Present STs are capable of generating toroidal flows approaching the ion sound speed which, according to previous theoretical work [22, 23], can stabilise the n = 1 internal kink mode associated with the sawtooth instability. The effect of toroidal rotation on sawtooth stability has been investigated in MAST [24] by comparing the dependence of sawtooth period on neutral beam heating power for injection co and counter to the plasma current in discharges with similar magnetic field, plasma current and shape. As the beam power, and hence the toroidal rotation, is increased in the co direction, the sawtooth period increases monotonically (Fig. 6). However, for counter-NBI the sawtooth period first decreases below that in Ohmically heated plasmas, before increasing again at higher injected power and hence toroidal flow velocity. This is in good accordance with results from JET [25]. The minimum in sawtooth period occurs when the sawtooth precursor frequency goes to zero (Fig. 7) at which point the rotation induced by the beam injection is balancing the intrinsic rotation of the mode at the ion diamagnetic frequency. Stability analyses of the ideal internal kink mode (n = 1) with respect to toroidal rotation at finite ion diamagnetic frequency, using the MISHKA-F code [26], show good agreement with MAST data [24]. Furthermore, it is found that stabilisation of the ideal n = 1 internal kink mode is determined by the magnitude of the rotation at the q = 1 surface, rather than the flow shear, in agreement with theoretical models for the flow stabilisation which are based on the centrifugal forces at the q = 1 rational surface [22]. Kinetic effects [27] may also play a role and are presently under investigation.

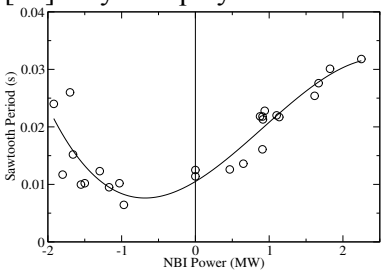

FIG. 6. Sawtooth period versus neutral beam power in MAST (-ve beam power denotes injection counter to I_p).

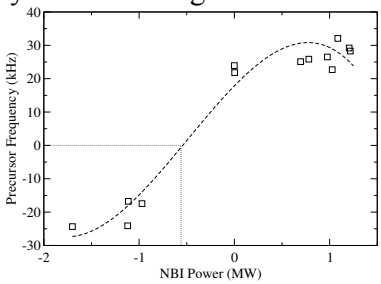

FIG. 7. Sawtooth precursor frequency versus neutral beam power in MAST (-ve precursor frequency corresponds to mode rotation in the counter-I_p direction).

4.3. Fast Particle Instabilities

Due to the low magnetic field in MAST, the fast ion population resulting from NBI is supra-Alfvénic, leading to excitation of a wide range of fast particle instabilities. Both 'perturbative' modes, which can be supported by the thermal plasma alone in the absence of fast particles, and 'non-perturbative' energetic particle modes, the dispersion properties of which are modified significantly by the fast ion population, are observed. At the levels observed so far Alfvén eigenmodes do not lead to any discernible degradation of confinement. On the other hand, non-perturbative modes such as 'fishbone instabilities' can be associated with a small reduction (a few %) in neutron emission. For TAEs and chirping modes, both the mode

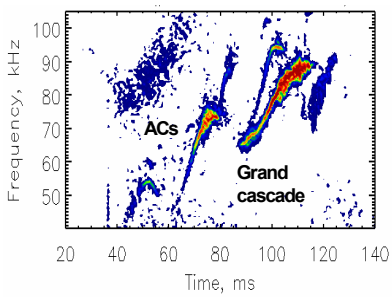

FIG. 8. Magnetic measurements showing the appearance of Alfvén cascades (discharge #16482).

amplitudes and the number of unstable modes are found to decrease with increasing beta [28]. Recent experiments have focussed on the study of 'Alfvén cascades' (ACs) [29], which are indicative of a non-monotonic q profile, to assess their characteristics and their potential as a diagnostic tool for magnetic shear reversal. At high power, strong chirping mode activity prevents observation of ACs. At low power (typically < 1.5MW), ACs have been observed in two different regimes: (i) early NBI together with a fast current ramp (5MA/s) and (ii) a two-step current ramp. An example from scenario (i) is illustrated in Fig. 8, where the grand cascade at ~90ms appears to be associated with $q_{min} = 3$. The NBI power in this case was ~600kW, supplied by the new PINI source. ACs have also been observed by interferometry and in some cases there are clear indications of ITB formation around the time of the cascade.

5. Plasma Exhaust

5.1. ELM and Pedestal Studies

ELM and pedestal studies have been extended to high temperature pedestal plasmas ($T_e^{ped} \leq 435eV$) with collisionalities $\nu_{ped}^* \sim 0.08$, one order of magnitude lower than in previous MAST experiments [30]. Pedestal widths in these low ν_{ped}^* plasmas are in better agreement with banana orbit scalings. Stability analysis, using the ELITE code, predicts broad mode structures and shows that the edge pressure gradient lies close to the ballooning limit, a characteristic usually associated with type I ELMs. The fraction of pedestal energy released by an ELM increases as the collisionality is decreased, as on other devices, reaching $\Delta W_{ELM} / W_{ped} \sim 12\%$, with peak power loads to the outboard divertor targets increasing up to 24 ± 4 MW/m^2. The fractional change in density pedestal during an ELM is effectively independent of the pre-crash pedestal conditions, and high spatial and temporal edge TS measurements show that the particle losses occur during the D_α rise. In contrast to observations at high pedestal collisionality, a substantial (50%) decrease in T_e^{ped} is measured during the ELM crash at low pedestal collisionality. Significant advances have been made in diagnosing the behaviour of ELM filament structures and understanding their role in the energy loss process [30, 31, 32]. High speed imaging (frame rates up to 200kHz) shows that the filaments are aligned with the local field lines, are characterised by a constant (in time) width perpendicular to the field lines of ~ 5 – 10cm and have a typical toroidal mode number n = 10-15. They remain close to the LCFS for 50-100μs, during which time most of the energy and particle loss (50 – 75%) occurs. All filaments initially rotate toroidally at the same velocity as the edge pedestal and then decelerate toroidally and accelerate radially outwards (Fig. 9). The filament characteristics (number,

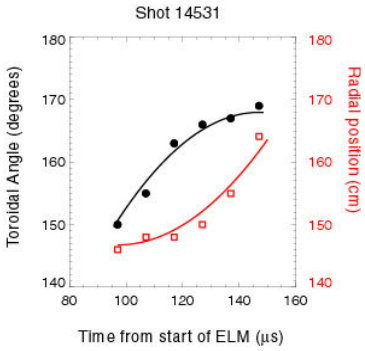

FIG. 9. The toroidal and radial location of one of the filaments, as a function of time during an ELM.

width) associated with type I ELMs are unchanged for an order of magnitude variation in ν^*_{ped}. Magnetic measurements indicate that the ELM filaments carry electrical current [32]. The edge TS system has been used to measure the evolution of density and temperature associated with individual filaments with a temporal resolution of 5μs (Fig. 10). At the time the filaments leave the LCFS, each one contains at most 2.5% of the particles and 1.5% of the energy expelled by the ELM. The radial acceleration of the filaments measured by the TS is in agreement with that measured by visible imaging. The ELM filament characteristics are consistent with the predictions of the nonlinear theory of the ballooning instability, at least during the initial growth [33].

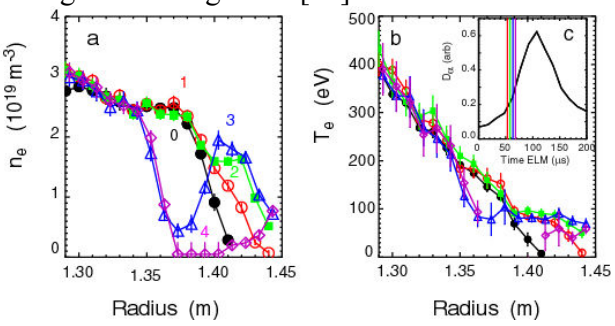

FIG. 10. Evolution of a) edge density profile and b) edge temperature profile for a single ELM. c) the target D_α signal versus time. 0) The solid black circles indicate the profile at the previous inter-ELM period. Profiles 1) red, 2) green, 3) blue and 4) purple are obtained at times of 53, 58, 63 and 68 μs from the start of the ELM (#14648).

5.2 L-mode Turbulence

In MAST L-mode plasmas [34], high speed imaging and edge TS also show the existence of filaments (Fig. 11), which have been shown to be correlated with the intermittent bursts on reciprocating probe data [32]. Intermittent transport, driven by these radially propagating plasma filaments, may play a key role in cross-field transport. The L-mode filaments initially have similar width (~5cm) to the type I ELM filaments and are also aligned along field lines. However, they have higher toroidal mode number (n = 30 – 50) and exhibit constant toroidal (typically ~ 3km/s) and radial (~ 1km/s) velocity. As they move outwards they tend to disperse and disintegrate into smaller structures. There is no observable magnetic signature associated with the L-mode filaments. The L-mode filament characteristics are consistent with those expected from an interchange instability [35]. BOUT simulations of MAST Ohmic plasmas have been performed for comparison with edge turbulence data [36]. These show electrostatic, high mode-number (n ~ 50) filaments ejected from the plasma edge into the SOL with widths ~6cm which then disintegrate, in broad agreement with observations. Powerful statistical techniques, which have been applied to edge Langmuir probe data in order to examine aggregate qualities of edge turbulence, have also been applied to virtual probe data calculated from the BOUT results. Differences are observed, primarily due to the lack of very small scale structures in BOUT, but the time-scales of the data associated with individual filaments are consistent. Both data and simulation show that fluctuations become more intermittent at smaller scales, possibly associated with the break-up of individual filaments.

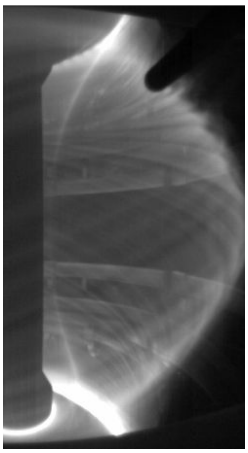

FIG. 11. Fast visible imaging (10,000fps, 20μs integration time) taken during a 0.8MA Ohmic L-mode double-null plasma (#15099).

5.3. Disruption Studies

The open structure of the MAST divertor, combined with the low aspect ratio geometry, provide an excellent opportunity to study transient power loads. The divertor targets are viewed with a fast infra-red camera (10kHz frame rate, 4μs integration time), filtered at 4.5 – 5.5μm to reduce the impact of surface effects and plasma radiation. Wide angle views, covering 70% of the vessel, are also available (at 315Hz frame rate, 1ms integration time), providing important information on poloidal and toroidal asymmetries. Analysis of data from more than 1000 disruptions shows that, on average, 55 % of the thermal energy in the plasma, W_{th}, is 'gradually' released over a period of up to 25ms immediately prior to the beginning of the plasma current redistribution (Fig. 12). This is well before the rapid loss of W_{th}, often characterised as the thermal quench, and acts to reduce the peak power load during the disruption, although small fluctuations in W_{th} during this early phase can result in substantial temporary excursions in the power load on the divertor. There is a substantial broadening of the divertor heat flux width during the thermal quench. Infra-red measurements show that the broadening is complex – spiral structures are observed during disruptions triggered by 'giant' sawteeth and locked modes (Fig. 13), whereas VDEs usually lead to a more homogeneous poloidal broadening [37]. In all cases substantial toroidal asymmetries can be observed. The observed spiral structures are reminiscent of those calculated and observed to occur in COMPASS-D [38] due to the application of resonant magnetic perturbations. MAST data on current quench timescales are incorporated in the ITER disruption database [39] and show that inductance effects due to plasma geometry should probably be included in any scalings.

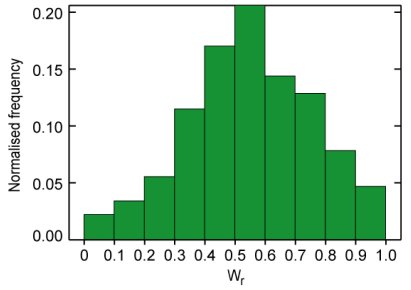

FIG. 12. Histogram showing the fraction, W_r, of plasma thermal energy remaining in the core just prior to the rapid thermal quench, compared to 20ms earlier, for ~1100 disruptions in MAST.

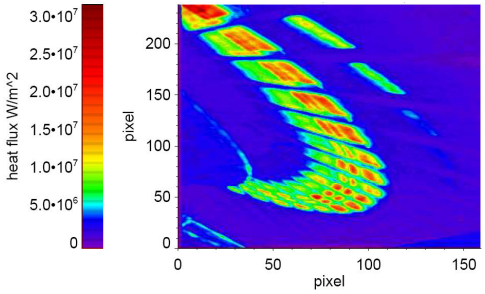

FIG 13. Infra-red measurements of heat flux to divertor following a disruption triggered by a large sawtooth (#11020).

6. Future Plans

Important physics advances have been made on MAST, of relevance to both STs and conventional tokamaks such as ITER, aided by further developments to diagnostics including high resolution CXRS, edge Thomson scattering, visible and infra-red imaging systems, edge probes, etc. First promising results have been obtained from the prototype MSE system, in collaboration with KTH Stockholm, justifying extension to a multi-channel system in 2007. Replacement of the short pulse NBI sources with long pulse JET-style PINI sources reached an important milestone with operation of the first PINI into plasma. In preparation for longer pulse operation, real-time equilibrium reconstruction has been implemented (RTEFIT). Further exciting developments are underway. An active TAE antenna array was installed in October 2006 and it is planned to extend this system to provide an ELM mitigation capability

in 2007. A dedicated EBW plasma start-up system (28GHz) is also being installed at present and plans for a high power, low frequency EBW heating and current drive system are being developed. The capabilities of our high resolution TS systems will be further extended. Longer term plans include installation of a new centre column (more inductive flux), a new cryo-pumped divertor and further enhancements to the NBI system, i.e. higher power with adaptable launch geometry (co/counter, core/off-axis). These developments will allow MAST to address the important questions relating to steady-state ST operation and further enhance its capability to contribute to key ITER physics issues.

Acknowledgements

This work was jointly funded by the UK Engineering and Physical Sciences Research Council and by the European communities under the Contract of Association between Euratom and UKAEA. The views and opinions expressed herein do not necessarily reflect those of the European Commission. NBI equipment is on loan from ORNL, the NPA from PPPL and the pellet injector was provided by FOM. Plasma control software was provided by GA. The authors gratefully acknowledge C. Petty (GA) for the provision of DIII-D data in support of confinement scaling studies.

References

[1] VALOVIC, M., et al., Nucl. Fusion **45** (2005) 942.
[2] KAYE, S. M., Plasma Phys. Control. Fusion **48** (2006) A429.
[3] FIELD, A. R., et al., Plasma Phys. Control. Fusion **46** (2004) 981.
[4] ROZHANSKY V., et al., Proc. 16th Int. PSI Conf., Portland, USA (2004) P2-57.
[5] MEYER, H., et al., Plasma Phys. Control. Fusion **47** (2005) 843.
[6] MEYER, H., et al., Nucl. Fusion **46** (2006) 64.
[7] MEYER, H., et al., Plasma Phys. Control. Fusion, submitted (2006).
[8] ROZHANSKY, V., et al., Plasma Phys. Control. Fusion **48** (2006) 1425.
[9] ANDREW, Y. et al., Plasma Phys. Control. Fusion **46** (2004) A87.
[10] AKERS, R., et al., Proc. 20th IAEA Fusion Energy Conf., Vilamoura, (2004) EX/4-4.
[11] CONNOR, J.W., et al., this conference (2006) Paper TH/P2-2.
[12] AXON, K., et al., Proc. 31st EPS Conf., London, UK (2006) P4-197.
[13] MILORA, S. L. & FOSTER, C. A., IEEE Trans. Plasma Sci. (1978) PS-6 578.
[14] PARKS, P. B. & TURNBULL, R. J., Phys. Fluids **21** (1978) 1735.
[15] AKERS, R., et al., this conference (2006) Paper EX/P3-13.
[16] TOURNIANSKI, M.R., et al., Plasma Phys. Control. Fusion **47** (2005) 671.
[17] TOURNIANSKI, M.R., et al., Proc. 33rd EPS Conf., Rome, Italy (2006) P1.099.
[18] SHEVCHENKO, V., et al., this conference (2006) Paper EX/P6-22.
[19] SURKOV, A., et al., Proc. 32nd EPS Conf., Tarragona, Spain (2005) P-5.103.
[20] ALLADIO, F., et al., Proc. 33rd EPS Conf., Rome, Italy (2006) P1.095.
[21] PINCHES, S.D. et al., this conference (2006) Paper EX/7-2Ra.
[22] WAELBROECK, F.L., Phys. Plasmas **3** (1996) 1047.
[23] WAHLBERG, C. & BONDESON, A., Phys. Plasmas **7** (2000) 923.
[24] CHAPMAN, I., et al., Nucl. Fus., submitted (2006).
[25] NAVE, M.F.F., et al., Phys. Plasmas **13** (2006) 014503.
[26] CHAPMAN, I., et al., Phys. Plasmas **13** (2006) 065211.
[27] GRAVES, J., et al., Phys. Plasmas, **10** (2003) 1034.
[28] GRYAZNEVICH, M. & SHARAPOV, S., Plasma Phys. Control. Fusion **46** (2004) S15.
[29] SHARAPOV, S.E. et al., Phys. Plasmas **9** (2002) 2027.
[30] KIRK, A., et al., this conference (2006) Paper EX/9-1.
[31] KIRK, A.., et al., Phys. Rev. Lett. **96** (2006) 185001.
[32] KIRK, A., et al., Plasma Phys. Control. Fusion, accepted for publication (2006).
[33] WILSON, H.R. & COWLEY, S.C., Phys. Rev. Lett. **92** (2004) 175006.
[34] COUNSELL, G.F., et al., this conference (2006) Paper EX/P4-6.
[35] GARCIA, O.E., et al., Phys. Plasmas **12** (2005) 062309.
[36] DUDSON, B., et al., Proc. 32nd EPS Conf., Tarragona, Spain (2005) O4.019.
[37] DELCHAMBRE, E., et al., Proc. 17th Int. PSI Conf., Hefei, China (2006) P3-52.
[38] BUTTERY, R.J., et al., Nucl. Fusion **36** (1996) 1369.
[39] WESLEY, J.C., et al., this conference (2006) Paper IT/P1-21.